A small and round heliosphere suggested by magnetohydrodynamic modelling of pick-up ions

Merav Opher [1,2 ✉], Abraham Loeb[2], James Drake[3] and Gabor Toth[4]

As the Sun moves through the surrounding partially ionized medium, neutral hydrogen atoms penetrate the heliosphere, and through charge exchange with the supersonic solar wind, create a population of hot pick-up ions (PUIs). Until recently, the consensus was that the shape of the heliosphere is comet-like. The termination shock crossing by Voyager 2 demonstrated that the heliosheath (the region of shocked solar wind) pressure is dominated by PUIs; however, the impact of the PUIs on the global structure of the heliosphere has not been explored. Here we use a novel magnetohydrodynamic model that treats the PUIs as a separate fluid from the thermal component of the solar wind. The depletion of PUIs, due to charge exchange with the neutral hydrogen atoms of the interstellar medium in the heliosheath, cools the heliosphere, 'deflating' it and leading to a narrower heliosheath and a smaller and rounder shape, confirming the shape suggested by Cassini observations. The new model reproduces both the properties of the PUIs, based on the New Horizons observations, and the solar wind ions, based on the Voyager 2 spacecraft observations as well as the solar-like magnetic field data outside the heliosphere at Voyager 1 and Voyager 2.

The shape of the heliosphere has been explored in the past six decades[1–3]. There was a consensus, since the pioneering work of Baranov and Malama[4], that the heliosphere shape is comet-like. More recently, this standard shape has been challenged by the realization that the solar magnetic field plays a crucial role in funnelling the heliosheath (HS) solar wind flow into two jet-like structures[5,6]. Cassini's observations of energetic neutral atoms further suggest that the heliosphere has no tail[7].

Previous three-dimensional models for the global structure of the heliosphere have followed the pick-up ions (PUIs) and the thermal cold solar wind plasma using a single-ion fluid approximation[5,8,9], assuming that the PUIs are immediately mixed into the ambient solar wind plasma. Here we present a novel three-dimensional multi-ion magnetohydrodynamic (MHD) model that treats the PUIs as a separate fluid. We solve the full set of fluid equations for both components (including separate energy and momentum equations[10]; see Methods).

New Horizons has recently been making the first direct observations of PUIs in the supersonic solar wind as far as 30 au (ref. [11]). One of the surprising results is that the PUI temperature is increasing with distance as $r^{0.68}$ (where r is the radial distance from the Sun) and the density of PUIs is decreasing as $r^{-0.6}$, less rapidly than the r^{-1} scaling expected from first-order approximations to the PUI mass loading[12]. The increase of PUI thermal pressure in the supersonic solar wind could be due to several reasons. Ref. [11] speculates that it is caused by co-rotating interaction regions that merge and drive compression and heating. On the basis of observations at 30 au and 38 au, the extrapolated temperature and density of PUIs at 90 au are 8.7×10^6 K and 2.2×10^{-4} cm^{-3}. These measurements indicate that the PUI thermal pressure is a substantial fraction of the ram pressure of the solar wind upstream of the termination shock (TS).

Owing to the uncertain interpretation, we adopt an ad hoc heating of the PUIs in the supersonic solar wind to bring their temperature close to 10^7 K upstream of the TS. This value is in agreement with previous work that reproduced the TS crossing[13]. Our model naturally reproduces the value of the density of the PUIs upstream of the TS (Supplementary Table 1 and Supplementary Fig. 1).

We run two cases. The reason for that is that the interstellar magnetic field (B_{ISM}) strength and direction is not well constrained. Case A has the B_{ISM} in the hydrogen deflection plane ($-34.7°$ and $57.9°$ in ecliptic latitude and longitude, respectively) as in our previous single-ion model[5]. Case B uses the B_{ISM} based on the location and the circularity of the Interstellar Boundary Explorer (IBEX) ribbon[14] ($-34.62°$ and $47.3°$ in ecliptic latitude and longitude, respectively). The strength of the B_{ISM} (at the outer boundary of the simulation at distances where the interstellar medium is not affected by the heliosphere anymore) is 4.4 μG for case A and 3.2 μG for case B. We cover the entire heliosphere with high grid resolution, including the heliospheric tail (with resolution of 3 au throughout the tail for case A and 2 au for case B until 400 au and 4 au until 600 au) and 1.5 au across the TS for case A (and 1.0 au for case B). We run both cases in a time-dependent fashion for 943.2 yr (corresponding to $N = 2,720,000$ iterations) for case A and 957.2 yr for case B (corresponding to $N = 2,443,000$ iterations). For comparison, it takes a year for the solar wind to reach the TS (100 au) with a velocity of 400 km s^{-1}. In the HS, the speeds are ~50 km s^{-1} and it takes 40 yr to traverse the size of the heliosphere, ~400 au. Details of the simulations and the two cases are in Methods.

Our model reproduces the jumps in density, velocity and thermal solar wind temperature as measured by Voyager 2 (V2) across the TS (Fig. 1). V2 crossed the TS three times (due to radial motions of the TS) and the shock compression ratio was weak (~2.3–2.4)[15]. The observed solar wind speed and density were $v_{SW} \approx 300$ km s^{-1} and $n_{SW} = 10^{-3}$ cm^{-3}. The observed temperature of the solar wind upstream of the TS was $T_{SW} \approx 10^4$ K. This temperature was found by V2 to be roughly constant at distances $r > 10$ au (ref. [16]). This value is larger than expected from the adiabatic expansion of the solar wind. The reason is most likely due to turbulence driven by waves generated by the pick-up process and isotropization of the interstellar PUIs in the solar wind[16,17]. Our model does not include turbulence, so the solar wind temperature declines adiabatically with radius (modified by charge exchange—see Supplementary Fig. 1). However, with our choice of the inner boundary value of $T_{SW} = 2.10^4$ K, it reaches the value of $T_{SW} \approx 10^4$ K, as observed upstream of the TS by V2. Since

¹Astronomy Department, Boston University, Boston, MA, USA. ²Institute of Theory and Computation, Harvard University, Cambridge, MA, USA. ³University of Maryland, College Park, MD, USA. ⁴University of Michigan, Ann Arbor, MI, USA. ✉e-mail: mopher@bu.edu
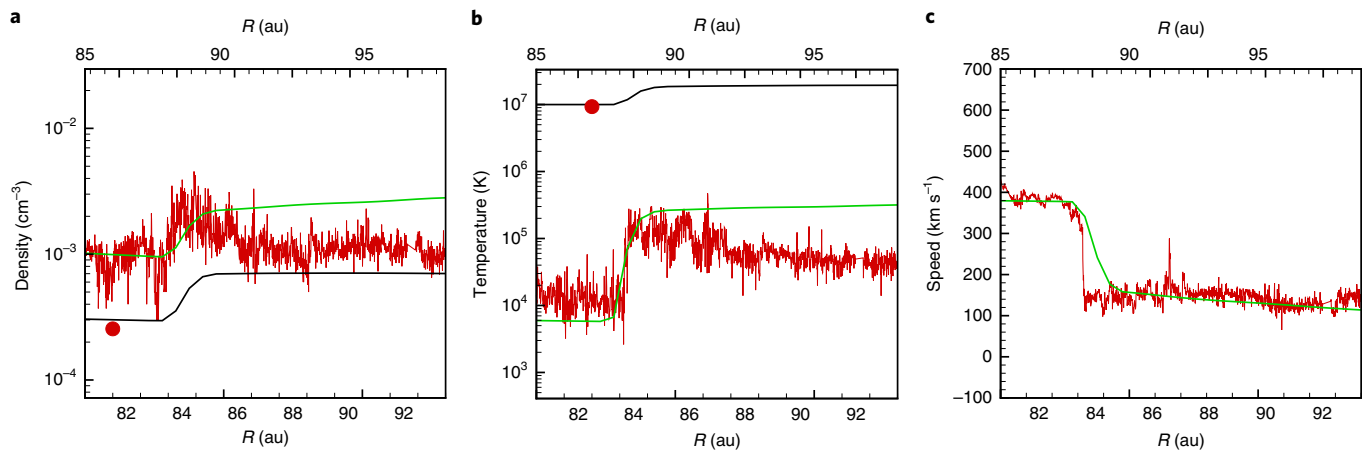
Fig. 1 | TS crossing at V2. a, Density. **b**, Temperature. **c**, Speed. The green line is the thermal solar wind component; the black line is the PUI component; the red line is the V2 measurements. The red dot indicates the values predicted upstream of the TS based on the measurements of New Horizon[11]. The bottom axis is the radial distance from the Sun as measured by V2 and the top axis as measured by the model (case B).

the solar wind thermal pressure is not the main pressure in the HS (its thermal energy density is an order of magnitude lower than the PUIs[13]), the investigation of the effects of turbulence is left for a future study.

As has been shown in local one-dimensional simulations[13,18,19], the PUIs carry most of the energy downstream of the TS and the HS thermal pressure is dominated by the PUIs and not by the thermal component (Supplementary Fig. 1). Our global model treats the crossing of the TS self-consistently by solving conservative equations for the separate ion fluids (Methods) that conserve mass, momentum and the hydrodynamic energy. This is a good approximation if the magnetic energy is small relative to the total energy density, which is true for the outer heliosphere. Owing to the fluid nature of our description, we are not able to capture kinetic effects such as shock acceleration of PUIs to higher energies, which can produce a non-negligible addition to pressure in the HS[20].

The presence of the PUIs as a separate fluid changes the energetics of the global HS and the overall structure of the heliosphere in two important ways. First, the PUIs weaken the TS by reducing the overall compression across the shock (Fig. 1). This means that the overall power going into the HS from the TS is smaller than in previous models. In addition, much of the energy that goes into the PUIs is eventually lost due to charge exchange with the interstellar neutrals downstream of the shock. As the PUIs charge exchange, they become energetic neutral atoms (ENAs) and leave the system because the mean free path of these particles is greater than the characteristic scale of the HS. This cools the HS much more quickly with distance downstream of the TS compared with the old model that treated the PUIs and the thermal components as a single fluid, where the loss of PUIs due to charge exchange was not included (Fig. 2b,e). The depletion of PUIs dramatically cools the outer heliosphere, 'deflating' it and leading to a smaller and rounder shape than previously predicted.

As a result of the weaker shock, the magnetic field in the HS just downstream of the TS is weaker than in the old single-ion models (Fig. 3d, dash-dotted lines). However, the drop in the PUI pressure leads to compression of the magnetic field further downstream of the TS. In the end, the magnetic field becomes enhanced, not at the shock but further downstream near the heliopause (HP; Fig. 3). The strong magnetic field near the HP means that the solar magnetic field continues to play a key role in controlling the overall shape of the heliosphere[5].

Second, the strong gradients of the PUI thermal pressure within the HS (Fig. 2b) drive faster flows to the north and south (Fig. 2a,d). As discussed by Drake et al.[6], the HS thickness is controlled by the continuity requirement: plasma flows across the TS must be balanced by flow down the tail within the HS. Stronger flows in the HS therefore reduce the thickness of the HS by deflating the heliospheric bubble and allowing the HS to be compressed by the interstellar medium (Fig. 3d).

The consequence of these two effects is a more 'squishable' heliosphere that has a smaller and rounder shape (Fig. 4a). This global structure is drastically different from the standard picture of a long heliosphere with a comet-like tail that extends to thousands of astronomical units (Fig. 4b). The distance from the Sun to the HP in the new round heliosphere is nearly the same in all directions. This new rounder and smaller shape is in agreement with the shape suggested by the ENA observations by the Cassini spacecraft[7]. The Cassini ENAs are produced by more energetic particles than the ones in our model, the 'core PUIs'. We can only gauge a limited depth of the HS, which happens to be rather short for ~1–6 keV (corresponding to the IBEX-Hi range of energy) and gets longer for energies <1 keV and >10 keV. One can observe farther down the tail at the higher energies measured by Cassini (5.5–55 keV). If the high-energy particles measured by Cassini imply a round heliosphere, the PUIs must also occupy a volume that is round since their loss mean free path is shorter than that of the energetic ions.

Our model predicts that PUIs stream with a higher velocity along magnetic field lines away from the nose of the HS than the solar wind ions (Fig. 3e). This large velocity is driven by the large drop in the PUI pressure towards the flanks (Fig. 3f). The motion of the thermal and PUI fluids perpendicular to the local magnetic field is controlled by the local electric field and is therefore the same for both species except in regions with large perpendicular gradients in pressure such as at the TS[13]. The perpendicular velocity of both species is therefore nearly the same over most of the region downstream of the TS (Supplementary Fig. 4). Along the magnetic field, however, the ion fluids are decoupled and can attain notably different velocities. In reality, two-stream instabilities restrict the relative ion velocities parallel to the magnetic field. These instabilities are a kinetic phenomenon that cannot be represented in multi-ion MHD. We therefore use a nonlinear artificial friction source term in the momentum equation to limit the relative velocities to realistic values (as in ref. [10]). This ad hoc artificial friction term in practice limits the velocity difference to the local Alfven speed (Methods).
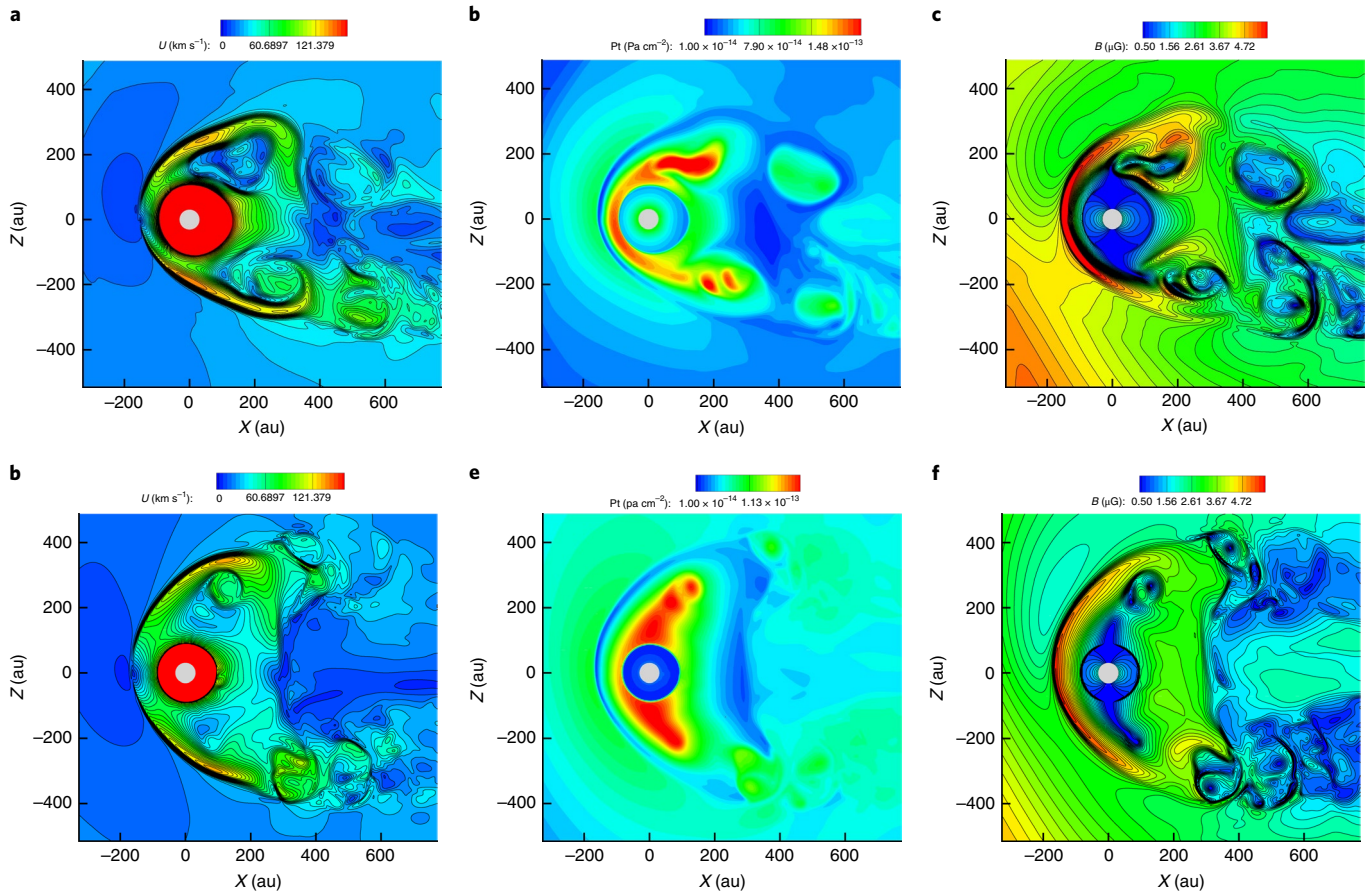
Fig. 2 | Meridional cuts showing the difference when PUIs and thermal ions are treated as separate fluids or not. a–f, Speed (*U*) (**a,d**), thermal pressure (Pt) (**b,e**) and magnetic field (*B*) (**c,f**) for the case when PUI and thermal ions are treated as separate fluids (case A) (**a–c**) and for the single ion (**d–f**).

Typically, the velocity difference between PUIs and solar wind is around 40 km s⁻¹ and is field-aligned (Fig. 3e).

The HS is dominated by thermal pressure almost all the way to the HP (Fig. 5 and Supplementary Fig. 2). Only near the HP is the magnetic pressure larger than the total thermal pressure. The temperature of the HS is dominated by the PUIs and is around 2 keV (Fig. 3g,h). The density of PUIs decreases with distance downstream of the TS in the HS (Fig. 3a) due to charge exchange. The spatial profile of the PUIs will affect the interpretation of the ENA maps measured at IBEX in the energy range of 1–4 keV.

Both Voyager spacecraft crossed the HP at roughly the same distance (~122 au for V1 and 119 au for V2[21]). The distances to the HP in the V1 and V2 directions in case B are comparable although both exceed the distances measured by the two spacecraft (Table 1).

One of the biggest surprises of both Voyager HP crossings is that the B_{ISM} did not change direction, in contrast with theoretical predictions. Some studies explain the V1 B_{ISM} direction as due to the location of V1 compared with the B_{ISM} (ref. [22]) or by time-dependent phenomena[23], but these explanations predict a field rotation at the V2 HP crossing that was not observed. Both at V1 and V2, the magnitude of *B* increased at the HP but the direction did not change[24]. V1 still observes solar-like B_{ISM} angles, 24 au from the HP[25]. Our case B simulation, with B_{ISM} along the centre of the IBEX ribbon[14], reproduces the V1 and V2[24] observations of the magnetic field outside the heliosphere (Fig. 6) while case A does not.

The current model suppresses reconnection in the nose while allowing it in the flanks. The agreement with the magnetic field at V1 and V2 seems to confirm the ideas that reconnection is suppressed in the nose of the heliosphere while occurring in the flanks[26], due to reconnection suppression from diamagnetic drifts.

All present models of the global heliosphere yield thicknesses of the HS that are substantially larger than measured by V1 and V2. The thickness of the HS in the new multi-ion MHD model is reduced compared with the single-ion case (Table 1) and other models. This is because the TS moves outward and the HP moves inward when compared with the simplified case where the PUIs and thermal plasma are treated as a single fluid (Fig. 2a,d and Table 1). Again, this is a result of the effective 'deflation' of the heliospheric bubble due to the charge-exchange losses of the PUIs. This effect was also seen in previous models that treated the PUI as a separate component[27].

In addition, in these new simulations, the thermal pressure of PUIs upstream of the TS is greater than in earlier single-ion models (Supplementary Fig. 2) (around 30% of the ram pressure, 2.6×10^{-14} ergs cm⁻³) while the solar wind thermal pressure is an order of magnitude smaller (1.1×10^{-16} ergs cm⁻³) than the ram pressure (8.3×10^{-14} ergs cm⁻³). The increased pressure of the PUIs pushes the TS outward in the new model. Case A predicts that at V1, the distance to the TS is 96 ± 3 au while at V2, it is 91 ± 3 au, so the asymmetry in the TS in our new multi-ion model is reduced from previous single-ion models[28]. The distances to the TS for case B are 90 ± 3 au and 88 ± 3 au at V1 and V2, respectively, and agree with the observations (95 au at V1 and 85 au at V2). On top of the change in shape, the thickness of the HS is reduced in this new multi-ion model.
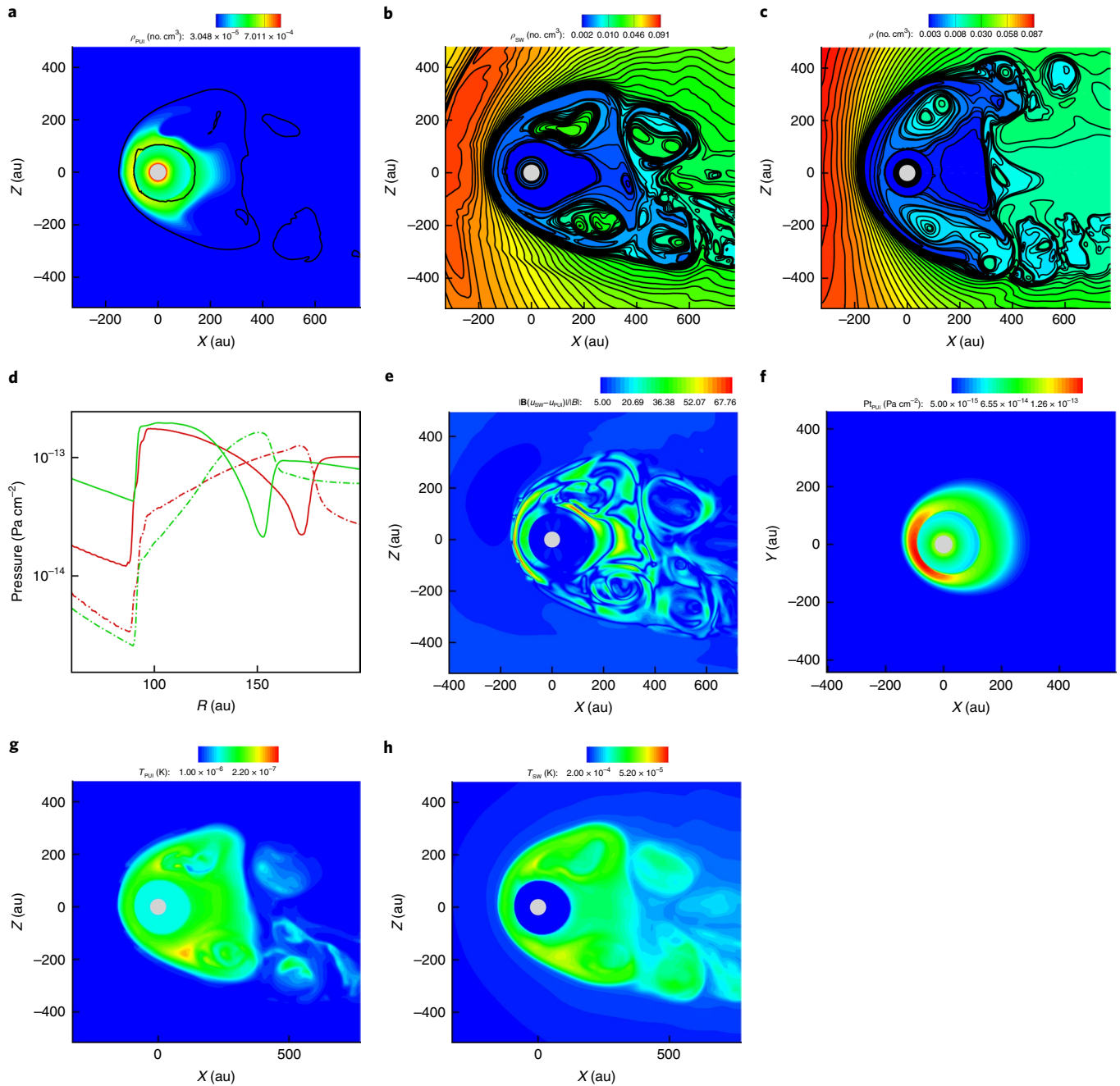
Fig. 3 | Density of PUIs and solar wind. a, The density of PUIs (ρ_{PUI}). Black contours show temperature at 0.25 MK indicating the HP. **b**, The density of the solar wind (ρ_{SW}). **c**, The density of the single fluid ion (PUIs and solar wind combined) model (ρ). **d**, Upstream cut showing the case with the multi-ion model in green and the single-ion model in red; the full lines are the thermal pressure and the dashed lines are the magnetic pressure. In the multi-ion case (model A), the thermal pressure is the total thermal pressure of the PUIs and the solar wind. Note that the single-ion case was shifted by 21 au. **e**, Field-aligned velocity difference between PUIs and solar wind is $|\mathbf{B}(u_{SW} - u_{PUI})|/|\mathbf{B}|$ in km s^{-1}. **f**, Thermal pressure of the PUIs in the equatorial plane (Pt$_{PUI}$). **g**, Temperature of PUIs (T_{PUI}). **h**, Temperature of the solar wind (T_{SW}).

Our new model does not include the solar cycle variation of the solar wind. However, time-dependent simulations[29] show that the TS only fluctuates by ± 10 au with the solar cycle, while fluctuations of the HP distance are only ~3–4 au. Thus, solar cycle variability cannot explain the continuing discrepancy between the thin HS measured by the Voyagers and the global models.

An important extension of this work would be to include not only the PUIs created in the supersonic solar wind (which peak around 1–3 keV) but also the higher-energy particles such as anomalous cos-

mic rays (ACRs) that are measured by V1 from 30 keV up to several megaelectronvolts. While none of the global models include ACRs, the diffusive loss of cosmic rays through the HP was predicted to shift the positions of the TS and HP by around 5 au (ref. [20]).

There have been suggestions that the inclusion of thermal conductivity[30], as well as an energy sink due to escaping ACRs, would reduce the HS thickness.

In future work, we will compare the ENA maps produced by this model with the ones observed by IBEX and the Ion and Neutral
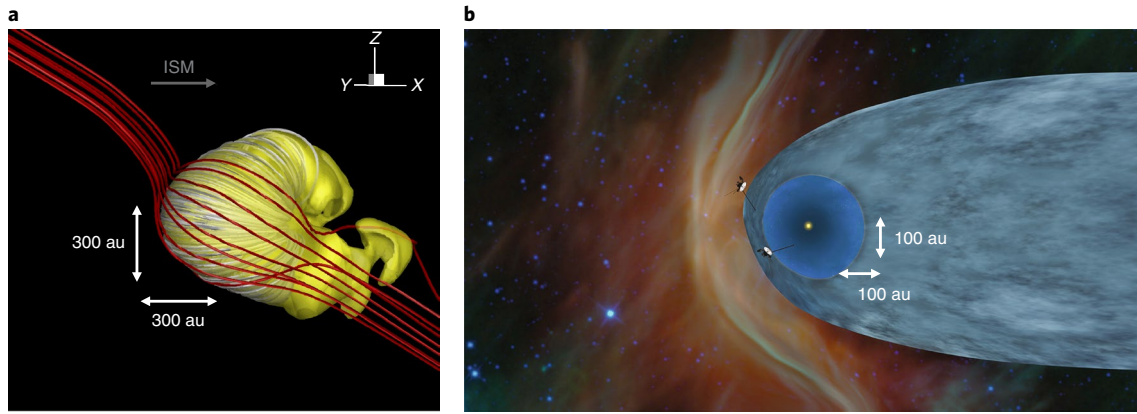
Fig. 4 | The new heliosphere. a, The HP is shown by the yellow surface (case B) defined by a solar wind density of 0.005 cm⁻³. The white lines represent the solar magnetic field. The red lines represent the interstellar magnetic field. **b**, The standard view of a comet long tail extending thousands of astronomical units. V1 and V2 are shown in this artist rendition; V2 has now passed the HP. The yellow dot represents the Sun. The supersonic solar wind region is represented by the blue region around the Sun. The extended region beyond the blue region represents the HS. Credit: NASA/JPL-Caltech.

Table 1 | Distances to TS and HP and the thickness of the HS

Case A			Case B	
	Single ion	Multi-ion	Multi-ion	Observations
TS (V1)	85 ± 3 au	96 ± 3 au	90 ± 3 au	95 au
HP (V1)	187 ± 3 au	171 ± 3 au	146 ± 3 au	122 au
HS (V1)	102 au	75 au	56 au	28 au
TS (V2)	80 ± 3 au	91 ± 3 au	88 ± 3 au	85 au
HP (V2)	162 ± 3 au	153 ± 3 au	141 ± 3 au	119 au
HS (V2)	82 au	62 au	53 au	35 au
HS (V1, V2)	20 au	13 au	3 au	7 au
TS (upwind)	82 ± 3 au	91 ± 3 au	85 ± 3 au	–
TS (downwind)	92 ± 3 au	123 ± 3 au	146 ± 3 au	–

The errors for the computed distances are taken as twice the local grid cell sizes.

Fig. 5 | Pressures in the HS. Pressures in the tail along a cut downstream (at $z = 0$) (case A). The red line is the PUI pressure; the blue line is the solar wind thermal pressure; the magenta line is the total thermal pressure (PUIs + solar wind); the green line is the magnetic pressure; and the black line is the total pressure (thermal + magnetic). The two grey vertical lines denote the positions of the TS (left) and the HP (right). R, radial distance from the Sun.

Camera (INCA)/Cassini. Our model includes the contribution from the thermal component and the 'core' PUIs. One can see that the model reproduces the ENA intensities at IBEX at energies of 0.5 keV–5 keV (Supplementary Fig. 5; when the HS-produced PUIs are included in post-processing). The model, similarly to other global models, does not reproduce the low-energy ENAs. There have been suggestions that effects beyond what ideal MHD description includes, such as turbulence[31] or reconnection, can contribute to such high intensities.

Future remote-sensing and in situ measurements will be able to test the reality of a rounder heliosphere. In Fig. 6, we show our prediction for the interstellar magnetic field ahead of the heliosphere at V2. In addition, future missions such as the Interstellar Mapping and Acceleration Probe[32] will return ENA maps at higher energies than present missions and so will be able to explore ENAs coming from deep into the heliospheric tail. Thus, further exploration of the

global structure of the heliosphere will be forthcoming and will put our model to the test.

Methods

Description of the governing equations. Our model has two ions, solar wind and PUIs interacting through charge exchange with neutral hydrogen atoms. The neutral hydrogen atoms are described in a multi-fluid treatment. There are four neutral populations, each reflecting the properties of the plasma between the different heliospheric boundaries[27].

The model assumes a 'cold electron' approximation, that is, that there are no suprathermal electrons. This is in agreement with the observations[15]. With n_{SW} and n_{PUI} being, respectively, the number density of the thermal solar wind protons and the PUIs, from charge neutrality we have the electron number density

$$n_e = n_{SW} + n_{PUI} \qquad (1)$$

where n_{SW} and n_{PUI} are the number density of SW and PUIs, respectively. Assuming that the electron and solar wind ion temperature are equal ($T_e = T_{SW}$), the solar wind thermal pressure is

$$p_{SW} = (n_{SW}T_{SW} + n_e T_e)k_B = (2n_{SW} + n_{PUI})T_{SW}k_B$$

where k_B is the Boltzmann constant. The PUI pressure is $p_{PUI} = n_{PUI}T_{PUI}k_B$.

We solve the multi-fluid set of equations (as in refs. [10,33]) for the solar wind and PUIs modified to include source terms due to charge exchange as in ref. [34]

$$\frac{\partial \rho_{SW}}{\partial t} + \boldsymbol{\nabla} \cdot (\rho_{SW}\mathbf{u}_{SW}) = S_{\rho_{SW}} \qquad (2)$$
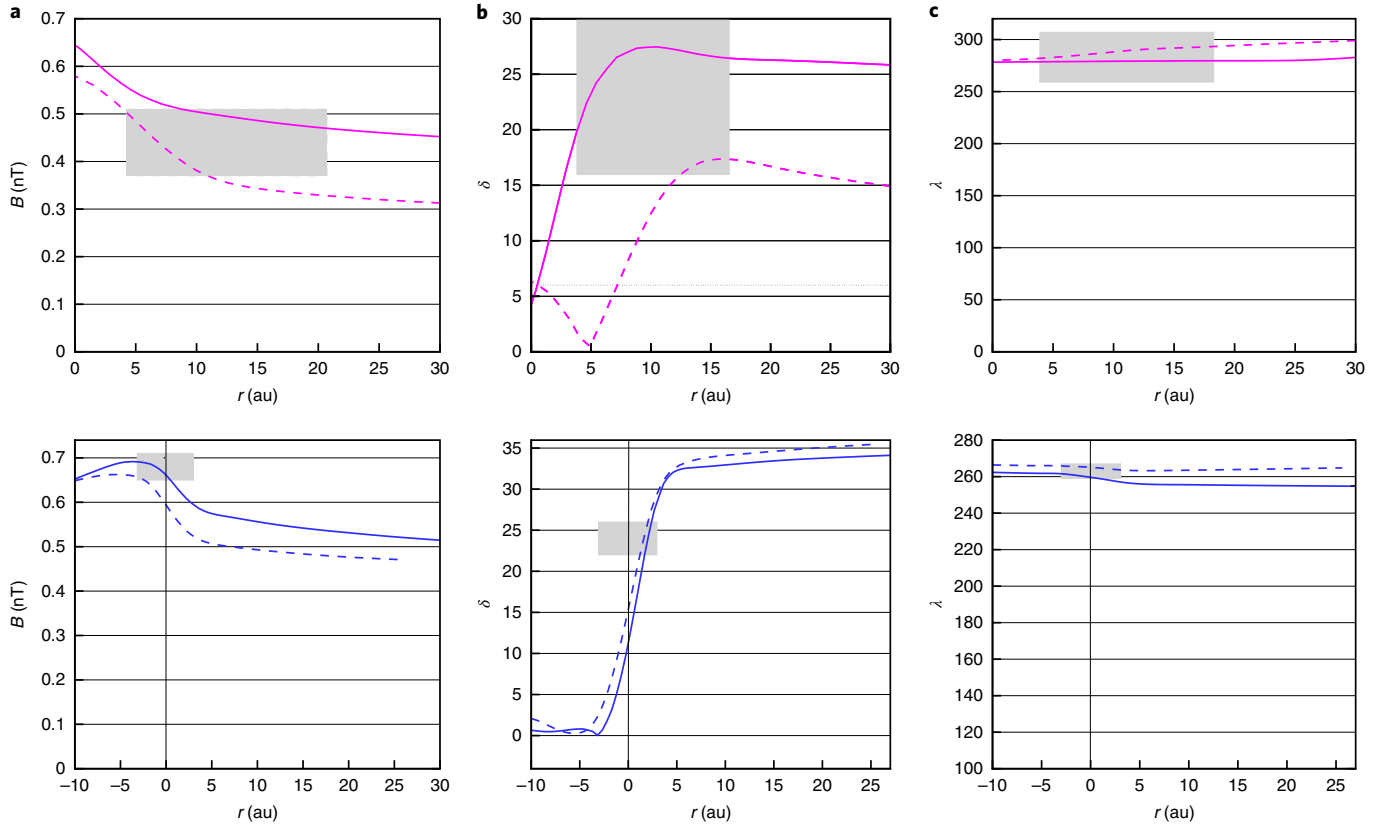
Fig. 6 | Magnetic field outside the HP at V1 and V2. a, The magnitude of the magnetic field. **b**, The angle $\delta = \sin^{-1}(B_N/B)$. **c**, The angle $\lambda = \tan^{-1}(B_T/B_R)$, where the *RTN* coordinate system is the local Cartesian system centred at the spacecraft. *R* is radially outward from the Sun, *T* is in parallel with the plane of the solar equator and is positive in the direction of solar rotation, and *N* completes a right-handed system for case B (full line) and case A (dashed line). The grey boxes are the observations[24] for V1 (top) and V2[21] (bottom). The variables are plotted versus the distance outside the HP at V1 and V2. The fast rise in angle *δ* for the first 10 au after the HP is due to interstellar magnetic field line causally connected (by Alfvén waves) to the solar magnetic field at the eastern flank by reconnection[25].

$$\frac{\partial \rho_{\mathrm{PUI}}}{\partial t} + \boldsymbol{\nabla} \cdot (\rho_{\mathrm{PUI}} \mathbf{u}_{\mathrm{PUI}}) = S_{\rho_{\mathrm{PUI}}} \tag{3}$$

$$\frac{\partial (\rho_{\mathrm{SW}} \mathbf{u}_{\mathrm{SW}})}{\partial t} + \boldsymbol{\nabla} \cdot \left(\rho_{\mathrm{SW}} \mathbf{u}_{\mathrm{SW}} \mathbf{u}_{\mathrm{SW}} + p_{\mathrm{SW}} \overleftrightarrow{I} \right) - \frac{\rho_{\mathrm{SW}}}{m_{\mathrm{p}}} (\mathbf{u}_{\mathrm{SW}} - \mathbf{u}_+)$$
$$\times \mathbf{B} - \frac{\rho_{\mathrm{SW}}}{n_e e} \mathbf{J} \times \mathbf{B} = S_{M_{\mathrm{SW}}} \tag{4}$$

$$\frac{\partial (\rho_{\mathrm{PUI}} \mathbf{u}_{\mathrm{PUI}})}{\partial t} + \boldsymbol{\nabla} \cdot \left(\rho_{\mathrm{PUI}} \mathbf{u}_{\mathrm{PUI}} \mathbf{u}_{\mathrm{PUI}} + p_{\mathrm{PUI}} \overleftrightarrow{I} \right) - \frac{\rho_{\mathrm{PUI}}}{m_{\mathrm{p}}} (\mathbf{u}_{\mathrm{PUI}} - \mathbf{u}_+) \times \mathbf{B} - \frac{\rho_{\mathrm{PUI}}}{n_e e}$$
$$\mathbf{J} \times \mathbf{B} = S_{M_{\mathrm{PUI}}} \tag{5}$$

$$\frac{\partial \mathcal{E}_{\mathrm{SW}}}{\partial t} + \boldsymbol{\nabla} \cdot [(\mathcal{E}_{\mathrm{SW}} + p_{\mathrm{SW}}) \mathbf{u}_{\mathrm{SW}}] - \frac{\rho_{\mathrm{SW}}}{m_{\mathrm{p}}} \mathbf{u}_{\mathrm{SW}} \cdot (\mathbf{u}_{\mathrm{SW}} - \mathbf{u}_+) \times \mathbf{B} - \frac{\rho_{\mathrm{SW}}}{n_e e} \mathbf{u}_{\mathrm{SW}}$$
$$\cdot \mathbf{J} \times \mathbf{B} = S_{\mathcal{E}_{\mathrm{SW}}} \tag{6}$$

$$\frac{\partial \mathcal{E}_{\mathrm{PUI}}}{\partial t} + \boldsymbol{\nabla} \cdot [(\mathcal{E}_{\mathrm{PUI}} + p_{\mathrm{PUI}}) \mathbf{u}_{\mathrm{PUI}}] - \frac{\rho_{\mathrm{PUI}}}{m_{\mathrm{p}}} \mathbf{u}_{\mathrm{PUI}} \cdot (\mathbf{u}_{\mathrm{PUI}} - \mathbf{u}_+)$$
$$\times \mathbf{B} - \frac{\rho_{\mathrm{PUI}}}{n_e e} \mathbf{u}_{\mathrm{PUI}} \cdot \mathbf{J} \times \mathbf{B} = S_{\mathcal{E}_{\mathrm{PUI}}} + H \tag{7}$$

where ρ_{SW} and ρ_{PUI} are the solar wind and PUIs mass densities, $\mathbf{u}_{\mathrm{SW}}$ and $\mathbf{u}_{\mathrm{PUI}}$ are the solar wind and PUI velocities, p_{SW} and p_{PUI} are the solar wind and PUI pressures, **E** and **B** are the electric and magnetic field strengths, **J** is the current density, $\overleftrightarrow{I}$ is the identity tensor and $\mathbf{u}_+ = \frac{\rho_{\mathrm{SW}} \mathbf{u}_{\mathrm{SW}} + \rho_{\mathrm{PUI}} \mathbf{u}_{\mathrm{PUI}}}{\rho_{\mathrm{SW}} + \rho_{\mathrm{PUI}}}$ is the charge-averaged ion velocity. ε is the hydrodynamic energy density, $\varepsilon = \rho\, \mathrm{u}^2/2 + \mathrm{p}/(\gamma - 1)$. The source terms denoted by $S_{\rho_{\mathrm{SW}}}, S_{M_{\mathrm{SW}}}, S_{\mathcal{E}_{\mathrm{SW}}}, S_{\rho_{\mathrm{PUI}}}, S_{M_{\mathrm{PUI}}}$ and $S_{\mathcal{E}_{\mathrm{PUI}}}$ represent the mass, momentum and energy sources for the solar wind ions and PUIs, respectively, due to charge exchange[34]. In equation (7), we include the possibility that the PUIs are heated in the supersonic solar wind with the heat source *H*. This is needed because observations by New Horizons[11] show that the PUIs are heated as a function of distance.

The approximately opposite effects of radiation pressure and gravity are neglected. Ionization processes, such as photoionization and electron-impact ionization, are also neglected. These processes play a much lesser role than charge exchange at larger radii ($R > 30$ au).

The neutral hydrogen atoms are described as four different neutral fluids having the characteristics of different regions of the heliosphere[28]. The four populations of neutral hydrogen atoms have different origins: atoms of interstellar origin represent population 4; population 1 is created by charge exchange in the region behind the interstellar bow shock (or slow bow shock[35]) and populations 3 and 2 originate from the supersonic solar wind and the HS, respectively. The four neutral populations indexed by $i = 1$–4 are described by separate systems of the Euler equations with the corresponding source terms describing the ion-neutral (both the solar wind and PUIs) charge-exchange process:

$$\frac{\partial \rho_{\mathrm{H}}(i)}{\partial t} + \boldsymbol{\nabla} \cdot (\rho_{\mathrm{H}} \mathbf{u}_{\mathrm{H}}) = S_{\rho_{\mathrm{H}}}(i) \tag{8}$$

$$\frac{\partial \rho_{\mathrm{H}} \mathbf{u}_{\mathrm{H}}}{\partial t} + \boldsymbol{\nabla} \cdot \left(\rho_{\mathrm{H}} \mathbf{u}_{\mathrm{H}} \mathbf{u}_{\mathrm{H}} + p_{\mathrm{H}} \overleftrightarrow{I} \right) = S_{M_{\mathrm{H}}}(i) \tag{9}$$

$$\frac{\partial \mathcal{E}_{\mathrm{H}}}{\partial t} + \boldsymbol{\nabla} \cdot [(\mathcal{E}_{\mathrm{H}} + p_{\mathrm{H}}) \mathbf{u}_{\mathrm{H}}] = S_{\mathcal{E}_{\mathrm{H}}}(i) \tag{10}$$

Source terms. We describe next, considering our multi-fluid description of the neutrals, which charge-exchange processes occur. In the supersonic solar wind (what we refer to as region 3), the following charge-exchange processes occur

$$p_0 + H_1 \rightarrow p_1 + H_3$$
$$p_0 + H_2 \rightarrow p_1 + H_3$$
$$p_0 + H_3 \rightarrow p_0 + H_3$$
$$p_0 + H_4 \rightarrow p_1 + H_3$$
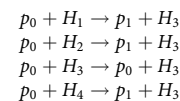
and

$$p_1 + H_1 \rightarrow p_1 + H_3$$
$$p_1 + H_2 \rightarrow p_1 + H_3$$
$$p_1 + H_3 \rightarrow p_0 + H_3 \quad \text{where } p_0 \text{ is the solar wind proton, } p_1 \text{ the PUI and } H_1, H_2,$$
$$p_1 + H_4 \rightarrow p_1 + H_3$$

H_3 and H_4 are, respectively, the neutrals of populations 1, 2, 3 and 4.

Outside of region 3, the following charge-exchange processes occur

$$p_0 + H_1 \rightarrow p_0 + H_2$$
$$p_0 + H_2 \rightarrow p_0 + H_2$$
$$p_0 + H_3 \rightarrow p_0 + H_2$$
$$p_0 + H_4 \rightarrow p_0 + H_2$$

and

$$p_1 + H_1 \rightarrow p_0 + H_2$$
$$p_1 + H_2 \rightarrow p_0 + H_2$$
$$p_1 + H_3 \rightarrow p_0 + H_2$$
$$p_1 + H_4 \rightarrow p_0 + H_2$$

Density source terms. In region 3, in the supersonic solar wind, the density source term for the solar wind protons is

$$S_{\rho_{SW}} = -\sum_{i=1}^{4} \rho_{SW} n_H(i) U^*(i) \sigma_{NSW}(i) + \rho_{SW} n_H(3) U^*(3) \sigma_{NSW}(3) \\ + \rho_{PUI} n_H(3) U^*_{PUI}(3) \sigma_{NPUI}(3) \tag{11}$$

and for the PUIs is

$$S_{\rho_{PUI}} = \sum_{i=1}^{4} \rho_{SW} n_H(i) U^*(i) \sigma_{NSW}(i) - \rho_{SW} n_H(3) U^*(3) \sigma_{NSW}(3) \\ - \rho_{PUI} n_H(3) U^*_{PUI}(3) \sigma_{NPUI}(3) \tag{12}$$

The source terms in density of the neutral populations $i = 1, 2, 4$ and Pop 3 are:

$$S_{\rho_H}(i) = -\rho_{SW} n_H(i) U^*(i) \sigma_{NSW}(i) - \rho_{PUI} n_H(i) U^*_{PUI}(i) \sigma_{NPUI}(i) \tag{13}$$

$$S_{\rho_H}(3) = \sum_{i=1}^{4} \rho_{SW} n_H(i) U^*(i) \sigma_{NSW}(i) + \sum_{i=1}^{4} \rho_{PUI} n_H(i) U^*_{PUI}(i) \sigma_{NPUI}(i) \\ - \rho_{SW} n_H(3) U^*(3) \sigma_{NSW}(3) - \rho_{PUI} n_H(3) U^*_{PUI}(3) \sigma_{NPUI}(3) \tag{14}$$

In region 2, in the HS, the density source term for the solar wind protons is

$$S_{\rho_{SW}} = \sum_{i=1}^{4} \rho_{PUI} n_H(i) U^*_{PUI}(i) \sigma_{NPUI}(i) \tag{15}$$

and for the PUIs is

$$S_{\rho_{PUI}} = -\sum_{i=1}^{4} \rho_{PUI} n_H(i) U^*_{PUI}(i) \sigma_{NPUI}(i) \tag{16}$$

The density source terms of the neutral populations $i = 1, 3, 4$ and Pop 2 are:

$$S_{\rho_H}(i) = -\rho_{SW} n_H(i) U^*(i) \sigma_{NSW}(i) - \rho_{PUI} n_H(i) U^*_{PUI}(i) \sigma_{NPUI}(i) \tag{17}$$

$$S_{\rho_H}(2) = \sum_{i=1}^{4} \rho_{SW} n_H(i) U^*(i) \sigma_{NSW}(i) + \sum_{i=1}^{4} \rho_{PUI} n_H(i) U^*_{PUI}(i) \sigma_{NPUI}(i) \tag{18}$$

Momentum source terms. In region 3, in the supersonic solar wind, the momentum source term for the solar wind protons is

$$S_{M_{SW}} = -\sum_{i=1}^{4} \rho_{SW} n_H(i) U^*_M(i) \sigma_{SW}(i) U_{SW} + \rho_{SW} n_H(3) U^*_M(3) \sigma_{SW}(3) U_H(3) \\ + \rho_{PUI} n_H(3) U^*_{M-PUI}(3) \sigma_{PUI}(3) U_H(3) \tag{19}$$

and for the PUIs is

$$S_{M_{PUI}} = \sum_{i=1}^{4} \rho_{PUI} n_H(i) U^*_M(i) \sigma_{SW}(i) \Delta U_{PUI-H}(i) + \sum_{i=1}^{4} \rho_{SW} n_H(i) U^*_M(i) \sigma_{SW}(i) \\ U_H(i) - \rho_{SW} n_H(3) U^*_M(3) \sigma_{SW}(3) U_H(3) - \rho_{PUI} n_H(3) U^*_{M-PUI}(3) \sigma_{PUI}(3) U_H(3) \tag{20}$$

The momentum source terms of the neutral populations $i = 1, 2, 4$ and Pop 3 are:

$$S_{M_H}(i) = -\rho_{SW} n_H(i) U^*_M(i) \sigma_{SW}(i) U_H(i) - \rho_{PUI} n_H(i) U^*_M(i) \sigma_{SW}(i) U_H(i) \tag{21}$$

$$S_{M_H}(3) = \sum_{i=1}^{4} \rho_{SW} n_H(i) U^*_M(i) \sigma_{SW}(i) U_{SW} + \sum_{i=1}^{4} \rho_{PUI} n_H(i) U^*_{M-PUI}(i) \sigma_{PUI}(i) U_{PUI} \\ - \rho_{SW} n_H(3) U^*_M(3) \sigma_{SW}(3) U_H(3) - \rho_{PUI} n_H(3) U^*_{M-PUI}(3) \sigma_{PUI}(3) U_H(3) \tag{22}$$

In region 2, in the HS, the momentum source term for the solar wind protons is

$$S_{M_{SW}} = \sum_{i=1}^{4} \rho_{SW} n_H(i) U^*_M(i) \sigma_{SW}(i) \Delta U_{SW-H}(i) \\ + \sum_{i=1}^{4} \rho_{PUI} n_H(i) U^*_{M-PUI}(i) \sigma_{PUI}(i) U_H(i) \tag{23}$$

and for the PUIs is

$$S_{M_{PUI}} = -\sum_{i=1}^{4} \rho_{PUI} n_H(i) U^*_{M-PUI}(i) \sigma_{PUI}(i) U_{PUI} \tag{24}$$

The momentum source terms of the neutral populations $i = 1, 3, 4$ and Pop 2 are:

$$S_{M_H}(i) = -\rho_{SW} n_H(i) U^*_M(i) \sigma U_H(i) - \rho_{PUI} n_H(i) U^*_M(i) \sigma U_H(i) \tag{25}$$

$$S_{M_H}(2) = \sum_{i=1}^{4} \rho_{SW} n_H(i) U^*_M(i) \sigma_{SW}(i) U_{SW} + \sum_{i=1}^{4} \rho_{PUI} n_H(i) U^*_{M-PUI}(i) \sigma_{PUI}(i) U_{PUI} \\ - \rho_{SW} n_H(2) U^*_M(2) \sigma_{SW}(2) U_H(2) - \rho_{PUI} n_H(2) U^*_{M-PUI}(2) \sigma_{PUI}(2) U_H(2) \tag{26}$$

Energy source terms. In region 3, in the supersonic solar wind, the energy source term for the solar wind protons is

$$S_{\mathcal{E}_{SW}} = -\sum_{i=1}^{4} [0.5 \rho_{SW} n_H(i) U^*_M(i) \sigma_{SW}(i) U^2_{SW} - \rho_{SW} n_H(i) U^*_M(3) \sigma_{SW}(3) U_{thSW}] \\ + 0.5 \rho_{SW} n_H(3) U^*_M(3) \sigma_{SW}(3) U^2_H(3) + \rho_{SW} n_H(3) U^*_M(3) \sigma_{SW}(3) U_{th}(3) \\ + 0.5 \rho_{PUI} n_H(3) U^*_{M-PUI}(3) \sigma_{PUI}(3) U^2_H(3) + \rho_{PUI} n_H(3) U^*_{M-PUI}(3) \sigma_{PUI}(3) U_{th}(3) \tag{27}$$

and for the PUIs is

$$S_{\mathcal{E}_{PUI}} = \sum_{i=1}^{4} 0.5 \rho_{PUI} n_H(i) U_M - PUI^*(i) \sigma_{PUI}(i) \left(U^2_H(i) - U^2_{PUI} \right) \\ + \sum_{i=1}^{4} \rho_{PUI} n_H(i) U_M - PUI^*(i) \sigma_{PUI}(i) (U_{th}(i) - U_{thPUI}) \\ - 0.5 \rho_{PUI} n_H(3) \sigma_{PUI}(3) U_M - PUI^*(3) U^2_H(3) \\ - \rho_{PUI} n_H(3) U_M - PUI^*(3) \sigma_{PUI}(3) U_{th}(3) + \sum_{i=1}^{4} [0.5 \rho_{SW} n_H(i) U^*_M(i) \sigma_{SW}(i) U^2_H(i) \\ + \rho_{SW} n_H(i) U^*_M(i) \sigma_{SW}(i) U_{th}(i)] - 0.5 \rho_{SW} n_H(3) U^*_M(3) \sigma_{SW}(3) U^2_H(3) \\ - \rho_{SW} n_H(3) U^*_M(3) \sigma_{SW}(3) U_{th}(3) \tag{28}$$

The energy source terms of the neutral populations $i = 1, 2, 4$ and Pop 3 are:

$$S_{\mathcal{E}_H}(i) = -0.5 \rho_{SW} n_H(i) U^*_M(i) \sigma_{SW}(i) U^2_H(i) - \rho_{SW} n_H(i) U^*_M(i) \sigma_{SW}(i) U_{th}(i) \\ - 0.5 \rho_{PUI} n_H(i) U^*_M(i) \sigma_{PUI}(i) U^2_H(i) - \rho_{PUI} n_H(i) U^*_M(i) \sigma_{PUI}(i) U_{th}(i) \tag{29}$$

$$S_{\mathcal{E}_H}(3) = -0.5 \rho_{SW} n_H(3) U^*_M(3) \sigma_{SW}(3) U^2_H(3) - \rho_{SW} n_H(3) U^*_M(3) \sigma_{SW}(i) U_{th}(3) \\ - 0.5 \rho_{PUI} n_H(3) U^*_{M-PUI}(3) \sigma_{PUI}(3) U^2_H(3) - \rho_{PUI} n_H(3) U^*_{M-PUI}(3) \sigma_{PUI}(3) U_{th}(3) \\ + \sum_{i=1}^{4} \left[\rho_{SW} n_H(i) U^*_M(i) \sigma_{SW}(i) U^2_{SW} + \rho_{SW} n_H(i) U^*_M(i) \sigma_{SW}(i) U_{thSW} \right] \\ + \sum_{i=1}^{4} \left[\rho_{PUI} n_H(i) U^*_{M-PUI}(i) \sigma_{PUI}(i) U^2_{PUI} + \rho_{PUI} n_H(i) U^*_{M-PUI}(i) \sigma_{PUI}(i) U_{thPUI} \right] \tag{30}$$

In region 2, in the HS, the energy source term for the solar wind protons is

$$S_{\mathcal{E}_{SW}} = \sum_{i=1}^{4} \left[0.5 \rho_{SW} n_H(i) U^*_M(i) \sigma_{SW}(i) (U^2_H(i) - U^2_{SW}) + \rho_{SW} n_H(i) U^*_M(i) \sigma_{SW}(i) \\ (U_{th}(i) - U_{thSW}) \right] + \sum_{i=1}^{4} \left[0.5 \rho_{PUI} n_H(i) U^*_{M-PUI}(i) \sigma_{PUI}(i) U^2_H(i) \\ + \rho_{PUI} n_H(i) U^*_{M-PUI}(i) \sigma_{PUI}(i) U_{th}(i) \right] \tag{31}$$

and for the PUIs is

$$S_{\mathcal{E}_{PUI}} = \sum_{i=1}^{4} \begin{bmatrix} -0.5 \rho_{PUI} n_H(i) U^*_{M-PUI}(i) \sigma_{PUI}(i) U^2_{PUI} \\ -\rho_{PUI} n_H(i) U^*_{M-PUI}(i) \sigma_{PUI}(i) U_{thPUI} \end{bmatrix} \tag{32}$$

The energy source terms of the neutral populations $i = 1, 3, 4$ and Pop 2 are:

$$S_{\mathcal{E}_H}(i) = -0.5 \rho_{SW} n_H(i) U^*_M(i) \sigma_{SW}(i) U^2_H(i) - \rho_{SW} n_H(i) U^*_M(i) \sigma_{SW}(i) U_{th}(i) \\ - 0.5 \rho_{PUI} n_H(i) U^*_{M-PUI}(i) \sigma_{PUI}(i) U^2_H(i) - \rho_{PUI} n_H(i) U^*_{M-PUI}(i) \sigma_{PUI}(i) U_{th}(i) \tag{33}$$

$$S_{\mathcal{E}_H}(2) = -0.5 \rho_{SW} n_H(2) U^*_M(2) \sigma_{SW}(2) U^2_H(2) - \rho_{SW} n_H(2) U^*_M(2) \sigma_{SW}(2) U_{th}(2) \\ - 0.5 \rho_{PUI} n_H(2) U^*_{M-PUI}(2) \sigma_{PUI}(2) U^2_H(2) - \rho_{PUI} n_H(2) U^*_{M-PUI}(2) \sigma_{PUI}(2) U_{th}(2) \\ + \sum_{i=1}^{4} \left[0.5 \rho_{SW} n_H(i) U^*_M(i) \sigma_{SW}(i) U^2_{SW} + \rho_{SW} n_H(i) U^*_M(i) \sigma_{SW}(i) U_{th}(i) \right] \\ + \sum_{i=1}^{4} \left[0.5 \rho_{PUI} n_H(i) U^*_{M-PUI}(i) \sigma_{PUI}(i) U^2_{PUI} + \rho_{PUI} n_H(i) U^*_{M-PUI}(i) \sigma_{PUI}(i) U_{thPUI} \right] \tag{34}$$

In the source terms, the following terms appear, where the index i refers to each population of neutrals 1, 2, 3 or 4. U_{thSW} is the thermal speeds of the solar wind and U_{thPUI} the thermal speed of PUIs:

$$U^*(i) = \sqrt{\frac{4}{\pi}\left(U_{thSW}^2 + U_{th}^2(i)\right) + \left(\Delta U_{SW-H}(i)\right)^2}, \ U_{thSW}^2 = \frac{2k_B T_{SW}}{m_p}, \ U_{th}^2(i)$$

$$= \frac{2k_B T_H(i)}{m_p}$$

$$U_{thPUI}^2 = \frac{2k_B T_{PUI}}{m_p}, \ U_{PUI}^*(i) = \sqrt{\frac{4}{\pi}\left(U_{thPUI}^2 + U_{th}^2(i)\right) + \left(\Delta U_{PUI-H}(i)\right)^2}$$

$$\Delta U_{SW-H}(i) = \sqrt{\mathbf{u}_H(i) - \mathbf{u}_{SW}}, \ \Delta U_{PUI-H}(i) = \sqrt{\mathbf{u}_H(i) - \mathbf{u}_{PUI}}$$

$$U_{M-PUI}^*(i) = \sqrt{\frac{64}{9\pi}\left(U_{thPUI}^2 + U_{th}^2(i)\right) + \left(\Delta U_{PUI-H}(i)\right)^2}$$

$$U_{M-SW}^*(i) = \sqrt{\frac{64}{9\pi}\left(U_{thSW}^2 + U_{th}^2(i)\right) + \left(\Delta U_{SW-H}(i)\right)^2}$$

The cross-sections are from ref. [36], where the uncertainties in the cross-sections are of ±10%. Recent studies[37] have investigated the effect of including different PUI distribution functions ('constructed' from the single-ion plasma distribution) in the computation of the charge-exchange source terms, which were subsequently applied to the single fluid MHD solver to obtain global heliospheric solutions that include the feedback of charge exchange with PUIs onto the plasma. Their conclusion is that despite differences in the charge-exchange source terms, the overall size of the heliosphere was similar and the differences in distances were less than 10%.

$$\sigma_{SW}(i) = \left(2.2835 \times 10^{-7} - 1.062 \times 10^{-8} \ln\left(U_{M-SW}^*(i) \times 100\right)\right)^2 \times 10^{-4} \ \text{cm}^2$$

$$\sigma_{NSW}(i) = \left(2.2835 \times 10^{-7} - 1.062 \times 10^{-8} \ln\left(U_{SW}^*(i) \times 100\right)\right)^2 \times 10^{-4} \ \text{cm}^2$$

$$\sigma_{PUI}(i) = \left(2.2835 \times 10^{-7} - 1.062 \times 10^{-8} \ln\left(U_{M-PUI}^*(i) \times 100\right)\right)^2 \times 10^{-4} \ \text{cm}^2$$

$$\sigma_{NPUI}(i) = \left(2.2835 \times 10^{-7} - 1.062 \times 10^{-8} \ln\left(U_{PUI}^*(i) \times 100\right)\right)^2 \times 10^{-4} \ \text{cm}^2$$

PUIs heating source term. The ad hoc heating source term H was chosen as

$$H = \rho_{PUI}\left(T_{PUI}(K) - 10^7 \ K\right)\left(r(au) - 30 \ au\right) \times 10 \tag{35}$$

only in the supersonic solar wind, where r is the radial distance and ρ_{PUI} and T_{PUI} are, respectively, the density and temperature of PUIs. This ad hoc heating brought the temperature of the PUI to 10^7 K upstream of the TS.

Numerical model. The inner boundary of our domain is a sphere at 30 au and the outer boundary is at $x = \pm 1,500$ au, $y = \pm 1,500$ au, $z = \pm 1,500$ au for case A and $x = \pm 1,500$ au, $y = \pm 2,000$ au, $z = \pm 2,000$ au for case B. We increased the grid size for case B to capture the slow bow shock[35] that forms along the plane that contains the interstellar magnetic field and interstellar velocity. Parameters of the solar wind at the inner boundary at 30 au were: $v_{SW} = 417$ km s^{-1}, $n_{SW} = 8.74 \times 10^{-3}$ cm^{-3} and $T_{SW} = 1.087 \times 10^5$ K (OMNI solar data; http://omniweb.gsfc.nasa.gov/). The magnetic field is given by the Parker spiral magnetic field with $B_{SW} = 7.17 \times 10^{-3}$ nT at the equator. We use a monopole configuration for the solar magnetic field. This description, while capturing the topology of the field line, does not include the change of polarity with solar cycle or across the heliospheric current sheet. This choice, however, minimizes artificial reconnection effects, especially in the heliospheric current sheet. In our simulation, we assume that the magnetic axis is aligned with the solar rotation axis. The solar wind flow at the inner boundary is assumed to be spherically symmetric. For the interstellar plasma, we assume: $v_{ISM} = 26.4$ km s^{-1}, $n_{ISM} = 0.06$ cm^{-3} and $T_{ISM} = 6,519$ K. The number density of hydrogen atoms in the interstellar medium is $n_H = 0.18$ cm^{-3}, the velocity and temperature are the same as for the interstellar plasma. The coordinate system is such that the Z axis is parallel to the solar rotation axis, the X axis is oriented in the direction of the interstellar flow (which points 5° upward in the X–Z plane) and the Y axis completes the right-handed coordinate system. The strength of the B_{ISM} in the model is 4.4 μG for case A and 3.2 μG for case B. The orientation of B_{ISM} continues to be debated in the literature. For case A, we use B_{ISM} in the hydrogen deflection plane (−34.7° and 57.9° in ecliptic latitude and longitude, respectively) consistent with the measurements of deflection of helium atoms with respect to the hydrogen atoms[38], and for case B, we use B_{ISM} used in studies that constrain

the orientation of B_{ISM} based on the location and circularity of the IBEX ribbon[14] (−34.62° and 47.3° in ecliptic latitude and longitude, respectively).

At the inner boundary (30 au), the density of the PUIs is set to $n_{PUI} = 9.45 \times 10^{-4}$ cm^{-3} so that the PUI density upstream of the TS at V2 corresponds to the predicted value by New Horizon (Fig. 4 and Supplementary Table 1). The temperature of the PUI at the inner boundary is chosen to be $T_{PUI} = 8.2 \times 10^6$ K. We introduce an ad hoc heating of the PUI, only in the supersonic solar wind, to bring their temperature to 10^7 K upstream of the TS as predicted by New Horizon. The value of the speed of the PUIs at the inner boundary is the same as the solar wind speed: $v_{PUI} = 417$ km s^{-1}.

Along the magnetic field, the PUI and solar wind fluids are decoupled and can attain different ion velocities in a cold electron approximation. In reality, two-stream instabilities physically restrict the relative ion velocities parallel to the magnetic field. This two-stream instability is a kinetic phenomenon that cannot be represented in multi-ion MHD; therefore, ref. [10] used a nonlinear artificial friction source term in the momentum equation to limit the relative velocities to realistic values

$$S_M^{friction} = \frac{\rho_{PUI}}{\tau_c}(\mathbf{u}_{PUI} - \mathbf{u}_{SW})\left(\frac{|\mathbf{u}_{PUI} - \mathbf{u}_{SW}|}{u_c}\right)^{\alpha_c} \tag{36}$$

where τ_c is the relaxation time scale, u_c is the cut-off velocity and α_c is the cut-off exponent. Here we used $\tau_c = 10^6$ s, $\alpha_c = 4$ and u_c is set to the local Alfvén speed using the total ion mass density.

Regarding the perpendicular speeds of PUIs and solar wind. The dominant terms in the PUI and SW momentum equations throughout most of the heliosphere are the terms proportional to $(\mathbf{u}_+) \times \mathbf{B}$ and $(\mathbf{u}_{SW}) \times \mathbf{B}$ or $(\mathbf{u}_{PUI}) \times \mathbf{B}$, where the first is basically the perpendicular electric field. These terms therefore typically balance so that the solar wind and PUI velocities are equal and given by the $\mathbf{E} \times \mathbf{B}$ drift. However, in regions where the local gradients in magnetic field or pressure are large, such as at the TS, other terms in the momentum equation can be significant and as a consequence the velocity of the ions can differ from the local $\mathbf{E} \times \mathbf{B}$ drift and from each other. For example, large gradients of PUI pressure can make the perpendicular speeds of the PUIs different than those of the solar wind ions. The term responsible for that, in the momentum equation, equation (5), is ∇p_{PUI}. Comparing that term with $\mathbf{u} \times \mathbf{B}$ the ratio is

$$\frac{\nabla p_{PUI}}{ne\mathbf{u} \times \mathbf{B}} \approx \frac{v_{diamag}}{U_{flow}} \approx \frac{v_{th(PUI)}}{U_{flow}}\frac{r_L}{L_p} \tag{37}$$

where $r_L = \frac{mv_{th(PUI)}}{|q|B}$ is the Larmor radius for the PUI, L_p is the characteristic length of the gradient of pressure, and v_{diamag} and $v_{th(PUI)}$ are, respectively, the diamagnetic and thermal speeds of the PUIs

$$v_{diamag} = \frac{v_{th(PUI)}}{L_p}\frac{mv_{th(PUI)}}{|q|B} \approx \frac{p_{PUI}}{n_{PUI}}\frac{1}{|q|BL_p}$$

The ratio in equation (37), $\frac{v_{th(PUI)}}{U_{flow}}$ ranges from ~7 in the mid-HS to ~30 near the HP.

$V_{th} \approx 4 \times 10^2$ km s^{-1} and $U_{flow} \approx 60$ km s^{-1}. The Larmor radii $r_L \approx 1.02 \times 10^{-3}$ $(T(K))^{1/2}B^{-1}$ km with $B \approx 0.34$ nT in the HS and $T \approx 10^7$ K for the PUIs

$$r_L \approx 2 \times 10^{-3} \ \text{au}$$

The PUI pressure drop length in the HS is $L_p \approx 25$ au. One can see that $\frac{\nabla p_{PUI}}{ne\mathbf{u} \times \mathbf{B}} \approx 6 \times 10^{-4}$ and the perpendicular speeds for the PUIs and solar wind ions should be the same. Supplementary Fig. 4 shows that the perpendicular speeds are, indeed, the same everywhere in the HS. At the TS, as shown in ref. [13], when L_p is small ($< r_L$) there should be a difference in the perpendicular speeds in PUI and solar wind.

Data availability
Our model is the OH module of SWMF and is available at http://csem.engin. umich.edu/tools/swmf/. The data produced by the model that support the findings of this study are available from the corresponding author upon reasonable request.

References
1. Davis, L. Interplanetary magnetic fields and cosmic rays. *Phys. Rev.* **100**, 1440–1444 (1955).
2. Parker, E. N. The stellar-wind regions. *Astrophys. J.* **134**, 20–27 (1961).
3. Axford, W. I. in *The Interaction of the Solar Wind with the Interstellar Medium* (eds Sonett, C. P. et al.) 609–660 (Scientific and Technical Information Office, NASA, 1972).
4. Baranov, V. B. & Malama, Y. G. Model of the solar wind interaction with the local interstellar medium: numerical solution of self-consistent problem. *J. Geophys. Res.* **98**, 15157–15163 (1993).

5. Opher, M., Drake, J. F., Zieger, B. & Gombosi, T. I. Magnetized jets driven by the Sun: the structure of the heliosphere revisited. *Astrophys. J.* **800**, L28 (2015).
6. Drake, J. F., Swisdak, M. & Opher, M. A model of the heliosphere with jets. *Astrophys. J.* **808**, L44 (2015).
7. Dialynas, K., Krimigis, S. M., Mitchell, D. G., Decker, R. B. & Roelof, E. C. The bubble-like shape of the heliosphere observed by Voyager and Cassini. *Nat. Astron.* **1**, 0115 (2017).
8. Izmodenov, V. V. & Alexashov, D. B. Three-dimensional kinetic-MHD model of the global heliosphere with the heliopause-surface fitting. *Astrophys. J. Suppl. Ser.* **220**, 32 (2015).
9. Pogorelov, N. V., Borovikov, S. N., Heerikhuisen, J. & Zhang, M. The heliotail. *Astrophys. J.* **812**, L6 (2015).
10. Glocer, A. et al. Multifluid block-adaptive-tree solar wind roe-type upwind scheme: magnetospheric composition and dynamics during geomagnetic storms—initial results. *J. Geophys. Res.* **114**, A12203 (2009).
11. McComas, D. et al. Interstellar pickup ion observations to 38 au. *Astrophys. J. Suppl. Ser.* **233**, 8 (2017).
12. Lee, M. et al. Physical processes in the outer heliosphere. *Space Sci. Rev.* **146**, 275–294 (2009).
13. Zieger, B., Opher, M., Toth, G., Decker, R. B. & Richardson, J. D. Constraining the pickup ion abundance and temperature through the multifluid reconstruction of the Voyager 2 termination shock crossing. *J. Geophys. Res.* **120**, 7130–7153 (2015).
14. Zirnstein, E. J. et al. Local interstellar magnetic field determined from the interstellar boundary explorer Ribbon. *Astrophys. J.* **818**, L18 (2016).
15. Richardson, J. D. et al. Cool heliosheath plasma and deceleration of the upstream solar wind at the termination shock. *Nature* **454**, 63–66 (2008).
16. Smith, C. W., Isenberg, P. A., Mathaeus, W. H. & Richardson, J. D. Turbulent heating of the solar wind by newborn interstellar pickup protons. *Astrophys. J.* **638**, 508–517 (2006).
17. Isenberg, P. A., Smith, C. W. & Matthaeus, W. H. Turbulent heating of the distant solar wind by interstellar pickup protons. *Astrophys. J.* **592**, 564–573 (2003).
18. Fahr, H. J. & Chalov, S. V. Supersonic solar wind ion flows downstream of the termination shock explained by a two-fluid shock model. *Astron. Astrophys.* **490**, L35–L38 (2008).
19. Zank, G. P. et al. Microstructure of the heliospheric termination shock: implications for energetic neutral atom observations. *Astrophys. J.* **708**, 1092–1106 (2010).
20. Guo, X., Florinski, V. & Wang, C. Effects of anomalous cosmic rays on the structure of the outer heliosphere. *Astrophys. J.* **859**, 157 (2018).
21. Richardson, J. D., Belcher, J. W., Garcia-Galindo, P. & Burlaga, L. F. Voyager 2 plasma observations of the heliopause and interstellar medium. *Nat. Astron.* **3**, 1019–1023 (2019).
22. Grygorczuk, J., Czechowski, A. & Grzedzielski, S. Why are the magnetic field directions measured by voyager 1 on both sides of the heliopause so similar? *Astrophys. J.* **789**, L43 (2014).
23. Pogorelov, N. V. et al. Heliosheath processes and the structure of the heliopause: modeling energetic particles, cosmic rays, and magnetic fields. *Space Sci. Rev.* **212**, 193–248 (2017).
24. Burlaga, L. F. et al. Magnetic field and particle measurements made by Voyager 2 at and near the heliopause. *Nat. Astron.* **3**, 1007–1012 (2019).
25. Burlaga, L. F., Florinski, V. & Ness, N. F. Turbulence in the outer heliosheath. *Astrophys. J.* **854**, 10 (2018).
26. Opher, M., Drake, J. F., Swisdak, M., Zieger, B. & Toth, G. The twist of the draped interstellar magnetic field ahead of the heliopause: a magnetic reconnection driven rotational discontinuity. *Astrophys. J.* **839**, L12 (2017).
27. Malama, Y. G., Izmodenov, V. V. & Chalov, S. V. Modeling of the heliospheric interface: multi-component nature of the heliospheric plasma. *Astron. Astrophys.* **445**, 693–701 (2006).
28. Opher, M. et al. A strong, highly-tilted interstellar magnetic field near the Solar System. *Nature* **462**, 1036–1038 (2009).
29. Izmodenov, V., Malama, Y. G. & Ruderman, M. S. Modeling of the outer heliosphere with the realistic solar cycle. *J. Adv. Space Res.* **41**, 318–324 (2008).
30. Izmodenov, V. V., Alexashov, D. B. & Ruderman, M. S. Electron thermal conduction as a possible physical mechanism to make the inner heliosheath thinner. *Astrophys. J.* **795**, L7 (2014).
31. Gloeckler, G. & Fisk, L. A. Proton velocity distributions in the inner heliosheath derived from energetic hydrogen atoms measured with Cassini and IBEX. *AIP Conf. Proc.* **1302**, 110–116 (2010).
32. McComas, D. J. et al. Interstellar mapping and acceleration probe (IMAP): a new NASA mission. *Space Sci. Rev.* **214**, 116 (2018).
33. Toth, G. et al. Adaptive numerical algorithms in space weather modeling. *J. Comput. Sci.* **231**, 870–903 (2012).
34. McNutt, R. L., Lyon, J. & Goodrich, C. C. Simulation of the heliosphere: model. *J. Geophys. Res.* **103**, 1905–1912 (1988).
35. Zieger, B., Opher, M., Schwadron, N. A., McComas, D. J. & Toth, G. A slow bow shock ahead of the heliosphere. *Geophys. Res. Lett.* **40**, 2923–2928 (2013).
36. Lindsay, B. G. & Stebbings, R. F. Charge transfer cross sections for energetic neutral atom data analysis. *J. Geophys. Res.* **110**, A12213 (2005).
37. Heerikhuisen, J., Zirnstein, E. J., Pogorelov, N. V., Zank, G. P. & Desai, M. Effects of suprathermal protons in the heliosheath on the global structure of the heliosphere and heliotail. *Astrophys. J.* **874**, 76 (2019).
38. Lallement, R. et al. Deflection of the interstellar neutral hydrogen flow across the heliospheric interface. *Science* **307**, 1447–1449 (2005).

Author contributions
M.O. performed the numerical simulations with guidance and collaboration from G.T. The scientific analysis and discussion of the results were done by all authors. The manuscript was reviewed and edited by all authors.

Competing interests
The authors declare no competing interests.

Additional information
Supplementary information is available for this paper at https://doi.org/10.1038/s41550-020-1036-0.

Correspondence and requests for materials should be addressed to M.O.

Reprints and permissions information is available at www.nature.com/reprints.

Publisher's note Springer Nature remains neutral with regard to jurisdictional claims in published maps and institutional affiliations.